ADVANCED ENERGY MATERIALS
www.advenergymat.de

Impact of PbI_2 Passivation and Grain Size Engineering in $CH_3NH_3PbI_3$ Solar Absorbers as Revealed by Carrier-Resolved Photo-Hall Technique

Julie Euvrard, Oki Gunawan, and David B. Mitzi**

With power conversion efficiencies now exceeding 25%, hybrid perovskite solar cells require deeper understanding of defects and processing to further approach the Shockley-Queisser limit. One approach for processing enhancement and defect reduction involves additive engineering—, e.g., addition of MASCN (MA = methylammonium) and excess PbI_2 have been shown to modify film grain structure and improve performance. However, the underlying impact of these additives on transport and recombination properties remains to be fully elucidated. In this study, a newly developed carrier-resolved photo-Hall (CRPH) characterization technique is used that gives access to both majority and minority carrier properties within the same sample and over a wide range of illumination conditions. CRPH measurements on n-type $MAPbI_3$ films reveal an order of magnitude increase in carrier recombination lifetime and electron density for 5% excess PbI_2 added to the precursor solution, with little change noted in electron and hole mobility values. Grain size variation (120–2100 nm) and MASCN addition induce no significant change in carrier-related parameters considered, highlighting the benign nature of the grain boundaries and that excess PbI_2 must predominantly passivate bulk defects rather than defects situated at grain boundaries. This study offers a unique picture of additive impact on $MAPbI_3$ optoelectronic properties as elucidated by the new CRPH approach.

1. Introduction

Metal-halide-based perovskite materials have attracted substantial attention over the last decade, driven in part by Pb-based systems that are promising for solar energy application. Most notably, the widely used $MAPbI_3$ (MA = $CH_3NH_3^+$) perovskite and related systems have exceeded initial expectations, with a remarkably defect tolerant electronic structure, resulting in a race for power conversion efficiencies (PCE) that approach the Shockley-Queisser limit.[1,2] As current PCE values exceed 25%, a deeper understanding of the mechanisms limiting efficiency is needed to further push the boundaries toward the theoretical limit. In this regard, the perovskite community has expended great efforts to optimize perovskite film morphology (e.g., film continuity and grain size), with the expectation that larger grain size should improve performance through reduced grain boundary recombination.[3,4] However, contradictory results, based on the evolution of solar cell performances with grain size (and associated grain boundary density), have appeared in the literature. While some studies report an increased PCE with increasing grain size,[5–7] Sherkar et al. have demonstrated that defects at grain boundaries in compact films are benign for solar cells under normal solar fluence levels due to their neutral nature when filled.[8] Density functional theory (DFT) and high-resolution imaging techniques have also been used to address the question of grain boundaries, but no agreement emerges from the different studies, as some reports suggest benign or beneficial grain boundaries[9,10] while others conclude that grain boundaries are detrimental for recombination.[11,12] The nature of grain boundaries is also reported to be dependent on the film growth conditions according to DFT calculations.[13] In an attempt to improve the solar cell performances, additive engineering has been developed to optimize the thin film morphologies, optoelectronic properties, and stability through the use of a growing range of additives including polymers, small molecules, metal or organic halide salts, inorganic acids, and nanoparticles.[3] Thiocyanate compounds such as methylammonium thiocyanate (MASCN) or lead thiocyanate ($Pb(SCN)_2$), for example, have been used to increase the grain size, but little is known about the impact of such additives on the optoelectronic properties of the perovskite layer.[14–16] Additionally, excess PbI_2 has been successfully introduced in $MAPbI_3$ films to improve the solar cell performances.[17–20] Some reports suggest that PbI_2

Dr. J. Euvrard, Prof. D. B. Mitzi
Department of Mechanical Engineering and Materials Science
Duke University
Durham, NC 27708, USA
E-mail: david.mitzi@duke.edu
Dr. O. Gunawan
IBM T. J. Watson Research Center
Yorktown Heights, New York, NY 10598, USA
E-mail: ogunawa@us.ibm.com
Prof. D. B. Mitzi
Department of Chemistry
Duke University
Durham, NC 27708, USA
The ORCID identification number(s) for the author(s) of this article can be found under https://doi.org/10.1002/aenm.201902706.

DOI: 10.1002/aenm.201902706

passivates defects at the grain boundaries, therefore decreasing the nonradiative recombination and increasing the carrier mobility.[21–23] According to DFT calculations, excess PbI_2 is also expected to have a self-doping effect on $MAPbI_3$, as has been experimentally observed through a shift of the Fermi level toward the conduction band.[24–27] Nevertheless, the role of excess PbI_2 in $MAPbI_3$ optoelectronic properties remains to be fully understood.

To improve our understanding of additive engineering—i.e., particularly the role of PbI_2 passivation, MASCN additive, grain size and grain boundaries on solar cell performance—we need to examine the perovskite film transport and recombination properties in more details. In this work, we use a newly developed carrier-resolved photo-Hall (CRPH) characterization technique using parallel dipole line ac Hall system.[28,29] This CRPH technique gives simultaneous access to both majority and minority carrier properties, including carrier recombination lifetime and diffusion length, all as a function of light intensity and including intensities comparable to 1 sun (the most important regime for solar application). Hall measurements carried out under illumination on halide perovskite films and crystals have been reported by Chen et al.[30] However, this earlier study reports the extraction of carrier recombination lifetime and diffusion length considering the Hall density extracted using the single carrier model (which is only valid in the dark). Under elevated light intensity, both electrons and holes must be accounted for in the calculation of excess carrier density and in the determination of minority carrier properties. In this study, we use a new equation derived by Gunawan et al.,[28] which enables the determination of excess carrier density as well as mobility for majority and minority carriers using light intensity-dependent photo Hall measurements. Hall measurements in perovskite films are generally very challenging due to the medium to low range mobility (≈10 $cm^2\ V^{-1}\ s^{-1}$) and very high sample resistance (>100 MΩ). We successfully obtain Hall signals from the perovskite samples over a wide ranging of light intensities using an ac magnetic field produced by a rotating parallel dipole line (PDL) Hall system followed by lock-in detection.[29] Using this carrier-resolved photo-Hall analysis technique, we obtain rich information regarding transport parameters from our samples, namely, carrier density, hole and electron mobility, carrier recombination lifetime and hole/electron/ambipolar diffusion lengths, under varying light intensity (photocarrier density), with varying grain size (tuned with MASCN and annealing temperature) and with/without addition of extra PbI_2. We show that extra PbI_2 induces defect passivation, improving the carrier recombination lifetime by one order of magnitude, as well as a slight n-doping effect. Transport and recombination properties are found to be nominally independent of grain size, thereby implying that PbI_2 passivation must primarily arise within the film bulk rather than at the grain boundaries (and also indicating that grain boundaries are nominally benign for the processing conditions used in this study). We discuss potential mechanisms responsible for improved lifetime by correlating our results with previous DFT studies.[24,25,31,32] Additionally, we show that the MASCN additive used to tune the grain size has no measurable impact on the optoelectronic properties of the $MAPbI_3$ films.

2. Results and Discussion

2.1. PbI_2 Passivation

As excess PbI_2 has been suggested to passivate defects at grain boundaries,[17,21,23] we first compare the evolution of electrical parameters with and without the addition of 5% extra PbI_2 in $MAPbI_3$ using CRPH measurements. An excess PbI_2 concentration of 5% is chosen as it led to improved solar cell performance in a recent study.[14] To avoid possible competing impacts of grain size and PbI_2 addition, we tune the grain size using the additive methylammonium thiocyanate (MASCN) and adjust its concentration (in mol%) to reach similar grain sizes with and without the extra PbI_2. MASCN has been demonstrated to help the formation of larger grains when added to the $MAPbI_3$ precursor solution.[14] Films processed using stoichiometric conditions (0% extra PbI_2) exhibit an average grain size of 600 ± 100 nm with 10% MASCN added. With the addition of 5% extra PbI_2, a concentration of 5% MASCN yields a similar average grain size of 800 ± 100 nm (see SEM comparison in **Figure 1**a,b). Therefore, we expect a limited impact of grain size between the two types of samples. It is worth mentioning that no phase associated with SCN is observed in XRD patterns (Figure 1c), suggesting that the additive does not substantially remain in the film after deposition and annealing. Additionally, Han et al.[14] showed that no residual SCN can be detected in the final film using depth profiling XPS and transmittance infrared measurements. They proposed that SCN^- and MA^+ react to form CH_3NH_2 and HSCN or CH_3SCN and NH_3 gases, all expected to leave the system during film formation. Moreover, we will later show in more detail that the use of MASCN additive has no experimentally significant impact on electrical parameters.

With the addition of 5% extra PbI_2, a secondary phase surrounding the perovskite grains appears in the SEM images (Figure 1b). Appearance of lighter colored grains in SEM images has already been reported for $MAPbI_3$ processed with excess PbI_2 or annealed at high temperature and has been attributed to the PbI_2 phase.[17,22,23,33] Energy-dispersive X-ray (EDX) analysis was performed on a sample with larger grain size (MASCN concentration of 10%) to facilitate the measurement and shows an evolution of the I/Pb atomic ratio from 2.78 ± 0.07 at the interior of the grains, consistent with $MAPbI_3$ phase, to 2.16 ± 0.09 on the lighter colored grains at the grain boundaries, consistent with PbI_2 phase. EDX results are summarized in Figure S1 and Table S1 (Supporting Information). XRD patterns with and without extra PbI_2 are given in Figure 1c). While the intensity of the peaks and the preferred orientation along the (110) axis are preserved, the addition of 5% extra PbI_2 leads to the formation of an additional peak at 12.7° corresponding to the PbI_2 phase. Therefore, SEM images and XRD patterns support the notion that a PbI_2 phase forms at the grain boundaries of $MAPbI_3$ when 5% extra PbI_2 is used in the precursor solution.

To determine the impact of extra PbI_2 on minority and majority carrier properties, we carried out CRPH measurement employing two samples per condition. A complete description of the CRPH technique has been recently reported by Gunawan et al.[28] The extraction of electrical parameters

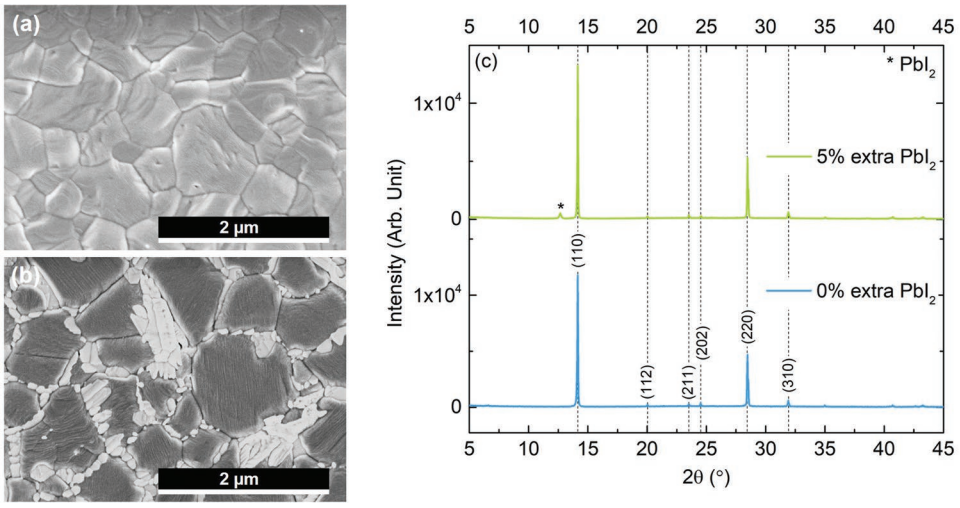

Figure 1. SEM images of the $MAPbI_3$ film surface processed with a) 0% extra PbI_2 (10% MASCN) and b) 5% extra PbI_2 (5% MASCN) using a magnification of 25kx. c) X-ray diffraction (XRD) spectra comparing the samples without extra PbI_2 (10% MASCN) and with 5% extra PbI_2 (5% MASCN).

for both electrons and holes relies on measuring the Hall coefficient H and conductivity σ at different light intensities, which varies by up to eight orders of magnitude. At any illumination, the conductivity and Hall coefficient depend on both electron and hole mobility and density, given by the following relations

$$\sigma = e\left(\mu_p p + \mu_n n\right) \tag{1}$$

$$H = \frac{r\left(p - \beta^2 n\right)}{e\left(p + \beta n\right)^2} \tag{2}$$

where e is the elementary charge, μ_p and μ_n are the hole and electron (drift) mobilities, p and n are the hole and electron densities, $\beta = \mu_n / \mu_p$ is the mobility ratio, and r is the Hall scattering factor, which can be considered equal to unity as commonly used in many Hall studies (this implies that the drift and Hall mobility are close or equal).[34]

Considering an n-type material, we have the total electron density $n = n_0 + \Delta n$ and the hole density $p = \Delta p$ where n_0 is the equilibrium or background electron carrier density in the dark. We assume equal photo carrier density for both electrons and holes $\Delta n = \Delta p$. With three unknowns (μ_p, μ_n, and Δn), Equations (1) and (2) cannot be solved at any given light intensity. To solve this problem, Gunawan et al.[28] have derived an equation independent of light intensity that yields an additional parameter $\Delta\mu_H$

$$\Delta\mu_H = d\left(\sigma^2 H\right)/d\sigma = \left(2 + \frac{dlnH}{dln\sigma}\right) H\sigma \tag{3}$$

where $\Delta\mu_H$ is the Hall mobility difference. The (drift) mobility difference is given as: $\Delta\mu = \mu_p - \mu_n = \Delta\mu_H / r$. Therefore, by measuring H and σ at variable light intensity and extracting the gradient of $\ln(H)$ with respect to $\ln(\sigma)$, it is possible to solve Equations (1), (2), and (3) at any given light intensity. We first solve for β as given in Table S1 (Supporting Information) of ref. [28]. Then, we can determine the hole mobility $\mu_p = \Delta\mu/(1-\beta)$, electron mobility $\mu_n = \beta\mu_p$, and the photo carrier density Δn at any light intensity, which is given as

$$\Delta n = \frac{\sigma(1-\beta) - e\Delta\mu n_0 \beta}{e\Delta\mu(1+\beta)} \left(\text{for } n-\text{type}\right) \tag{4}$$

Figure 2 displays the evolution of the Hall coefficient H with respect to the layer conductivity σ for one set of samples processed with and without extra PbI_2. To extract the $\Delta\mu$ value necessary to resolve the photo-Hall equations, the slope $d\ln(H)/d\ln(\sigma)$ is extracted from the H-σ plot using a logarithmic scale. Hall coefficients measured for both thin films at and near dark conditions are negative, indicating that the $MAPbI_3$ films in the current study are n-type with and without extra PbI_2, contrary to the p-type character for the $MAPbI_3$ films (prepared using a different approach) studied during a recent photo-Hall experiment.[28] It is worth noting that these results correspond to the first n-type materials characterized with the CRPH measurement, confirming the ability of the technique to study both types of semiconductors with low carrier densities. With $d\ln(H)/d\ln(\sigma)$ values between −1.09 and −1.3, and using Equation (3) we obtain negative $\Delta\mu$ values and therefore $\mu_n > \mu_p$. An example of the Hall coefficient measurement using ac field PDL Hall system is given in Figure S2 (Supporting Information). As can be observed in Figure S2e (Supporting Information), the Hall signal recorded over 15 min lock in detection stabilizes after 300–400 s, and it is from this region of the measurement that the Hall coefficient is extracted. Moreover, to exclude possible light-induced ion migration effects, we have measured the sheet resistance from low to high and back to low light intensities. The corresponding data are displayed in Figure S3 (Supporting Information) and exhibit a low level of hysteresis, suggesting a negligible impact of ion migration.

The evolution of μ_n, μ_p, and Δn and the Hall density n_{Hall} with the generation rate G (or incident light intensity) for $MAPbI_3$ processed with and without extra PbI_2 are shown in **Figure 3** for one sample each. Here we assume that the generation rate G is equal to the absorbed photon density G_γ, which implies

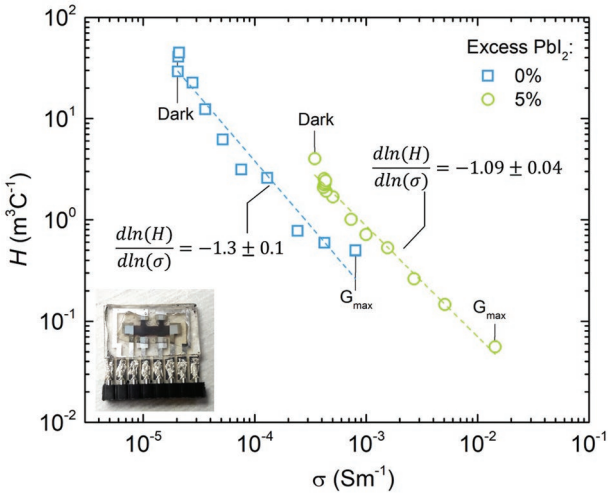

Figure 2. Carrier-resolved photo Hall H-σ plot for $MAPbI_3$ processed without extra PbI_2 (10% MASCN) and with 5% extra PbI_2 (5% MASCN). A picture of the encapsulated Hall bar is given as inset.

a photogeneration quantum efficiency equal to unity. Details about the calculation of the generation rate G can be found in a previous study.[28] The electron and hole mobilities are constant over the range of light intensities studied and therefore exhibit a slightly different behavior from the p-type films previously measured by Gunawan et al.,[28] for which a mobility increase is reported with increasing light intensity. The average electron mobilities μ_n, with values of 21 ± 9 and 20 ± 4 $cm^2\ V^{-1}\ s^{-1}$ without and with extra PbI_2 respectively, are slightly higher than the average hole mobilities μ_p of 14 ± 5 and 12 ± 4 $cm^2\ V^{-1}\ s^{-1}$, respectively. The mobilities obtained in our study are consistent with values reported in the literature for $MAPbI_3$.[35] The similar values obtained for μ_n and μ_p with and without extra PbI_2 suggest that no change related to shallow traps is induced by the PbI_2 phase at the grain boundaries or in the bulk. This observation is in general agreement with the slow decrease in mobility with excess PbI_2 suggested by the Hall measurements performed by Wang et al.,[27] but in contradiction with the Hall mobility increase measured after a 145 °C anneal by Shan et al.[22] As $MAPbI_3$ thin films decompose around 150 °C,[36] it is possible that new defects or enhancements in the crystalline quality arise in the film due to the higher temperature treatment, thereby changing the mobility of the layer in the Shan et al. study.

The Hall density n_{Hall} is extracted at each light intensity following the standard Hall relation for a single carrier: $n = -r/He$. For generation rates lower than ≈10^{18} $cm^{-3}\ s^{-1}$, n_{Hall} remains approximately constant and equal to the equilibrium electron density measured in the dark. Equilibrium carrier densities of $(1.0 \pm 0.2) \times 10^{11}$ cm^{-3} and $(2.6 \pm 0.1) \times 10^{12}$ cm^{-3} are obtained for $MAPbI_3$ processed under stoichiometric conditions and with 5% extra PbI_2, respectively. The density values are obtained from the average in the low light intensity region, where the measured n_{Hall} is approximately constant, and with error bars correspond to standard deviation. Considering an effective density of states in the conduction band N_c of 1.44×10^{18} cm^{-3},[37] it is possible to determine the position of the Fermi level in the bandgap. The electron densities obtained without and with 5% extra PbI_2 suggest a Fermi level shift by 90 meV, moving from 430 to 340 meV below the conduction band upon extra PbI_2 addition. The position of the Fermi level deduced from the carrier density under stoichiometric conditions is consistent with the values measured by Endres et al. using UPS and IPES on $MAPbI_3$.[38] A shift of the Fermi level toward the conduction band with PbI_2 excess has been previously observed experimentally using scanning tunneling spectroscopy and UPS.[27,39] Using DFT calculations, Yin et al.[24] and Kim et al.[25] have shown that $MAPbI_3$ should be tunable from p-type to n-type by changing the growth conditions and, therefore, the chemical potential of the components. Under Pb rich/I poor conditions, for example, MA interstitials and iodine vacancies exhibit the lowest formation energies, leading to n-doping with the formation of donor levels close to the conduction band.[24] Iodine vacancies responsible for n-doping have been shown to exhibit a low formation energy both for PbI_2-rich/MAI-poor and MAI-rich/PbI_2-poor conditions.[40] Regardless of the specific defects, the presence of 5% extra PbI_2 in the precursor solution impacts the chemical potential of constituents during film formation and therefore likely the formation energy and density of point defects associated with n-type doping. A substantial doping effect upon precursor ratio variation is, however, expected to be challenging due to the tendency of $MAPbI_3$ to compensate charged defects.[40–42]

At high light intensity, we observe a strong increase of n_{Hall} in Figure 3a, as the standard Hall equation does not take into

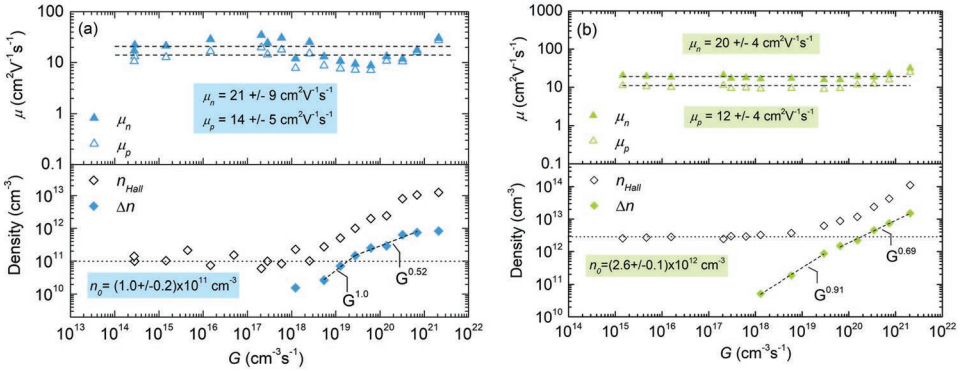

Figure 3. Electron μ_n and hole μ_p mobility, Hall density $n_{Hall,}$ and photocarrier density Δn as a function of generation rate G for $MAPbI_3$ processed a) without extra PbI_2 (10% MASCN) and b) with 5% extra PbI_2 (5% MASCN).

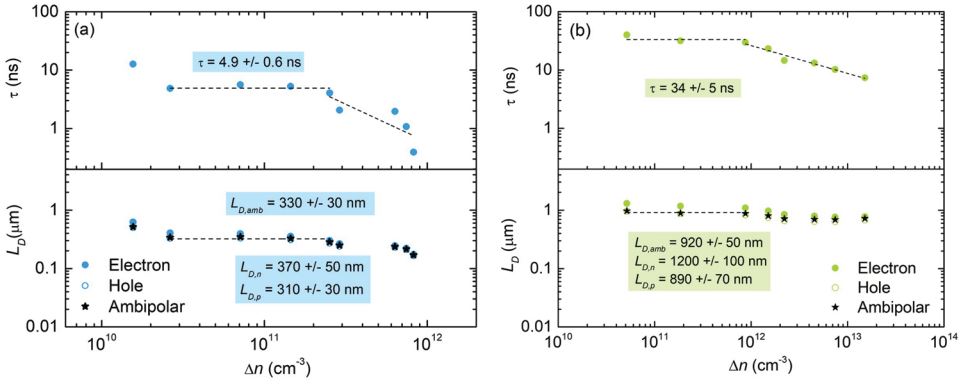

Figure 4. Carrier recombination lifetime τ, electron $L_{D,n}$, hole $L_{D,p,}$ and ambipolar $L_{D,amb}$ diffusion lengths as a function of excess carrier density Δ_n for $MAPbI_3$ processed a) without extra PbI_2 (10% MASCN) and b) with 5% extra PbI_2 (5% MASCN).

account both types of carriers. Indeed, for $\mu_n \approx \mu_p$ as observed with our samples, n_{Hall} is expected to diverge toward $+\infty$ with increasing generation rate (see Supporting Information). To properly follow the carrier density at high light intensity, it is important to calculate the excess or photo carrier density Δn obtained from Equation (4) for an n-type material. The excess carrier density is plotted with respect to the generation rate in Figure 3. The determination of the power law describing $\Delta n \propto G^{\alpha}$ is limited by the amount of data points collected and the uncertainty in the Δn evolution. Nevertheless, we can identify a possible gradual transition from a linear to a sublinear evolution with Δn as G reaches 10^{19}–10^{20} cm^{-3} s^{-1}. Bimolecular recombination dominating over trap-assisted recombination would lead to $\alpha = 0.5$. Moreover, Levine et al. show that a coefficient α ranging from 0 to 1 can be attributed to trap-assisted recombination when trap states are progressively filled and $n >> p$ for an n-type material.[35] It is unclear which regimes are observed in Figure 3 as $\Delta n \approx n_0$ and therefore $n \approx p$. Nevertheless, if we extract a bimolecular recombination constant k_2 from the $\Delta n \propto G^{0.5}$ regime in Figure 3a, we obtain a value of $(1.1 \pm 0.2) \times 10^{-3}$ cm^{-3} s^{-1}, about seven orders of magnitude higher than the value expected for $MAPbI_3$ films.[43] Therefore, it is more likely that the sublinear regime of Δn evolution with G is due to trap-assisted recombination. Assuming that this hypothesis is true, the trap density for these thin films would be higher than 4×10^{13} cm^{-3}, which is consistent with reported trap densities of 10^{16} to 10^{17} cm^{-3}.[44,45]

The excess carrier density and electron and hole mobilities can be used to calculate the carrier recombination lifetime $\tau = \Delta n/G$ and diffusion lengths for both electrons and holes

$$L_{D,n/p} = \sqrt{\frac{k_B T}{e} \mu_{n/p} \tau} \quad (5)$$

with k_B the Boltzmann constant and T the temperature. It is also possible to calculate the ambipolar diffusion length, $L_{D,amb} = \sqrt{D_{amb}\tau}$, which takes into account the collective diffusive behavior of both carriers and where D_{amb} is the ambipolar diffusion coefficient given by the following relation[46]

$$D_{amb} = \frac{k_B T}{e} \frac{n+p}{\frac{p}{\mu_n} + \frac{n}{\mu_p}} \quad (6)$$

The evolution of τ, $L_{D,p}$, $L_{D,n}$, and $L_{D,amb}$ with Δn for $MAPbI_3$ processed for the stoichiometric condition and with 5% extra PbI_2 appears in **Figure 4**. It is important to note that lifetime and ambipolar diffusion lengths should be calculated using Δn rather than n_{Hall}. As mentioned previously, n_{Hall} is expected to diverge when $\mu_p \approx \mu_n$, leading to an overestimation of the lifetime by several orders of magnitude (possibly accounting for the lifetime of 30 µs extracted by Hall measurements under illumination by Chen et al. for $MAPbI_3$ thin films).[30] Considering Δn, we obtain a lifetime of 4.9 ± 0.6 ns for the stoichiometric condition and observe an increase by approximately one order of magnitude to 34 ± 5 ns with the addition of 5% extra PbI_2. These values are obtained from the average in the regime where τ is constant with Δn. At high light intensities, τ follows a decreasing trend consistent with the sublinear dependency of Δn with G. The maximum light intensity of 30 mW cm^{-2} used in this experiment is approximately a third of one sun intensity (100 mW cm^{-2}). Therefore, we can expect the carrier recombination lifetime in a working solar cell to be slightly lower than the values reported, with the extent of the decrease depending on the $\Delta n \propto G^{\alpha}$ power law in this regime. Nevertheless, our results are consistent with the increase in carrier recombination lifetime upon addition of extra PbI_2 reported in the literature and suggest the passivation of deep traps.[17,21–23,47] The diffusion lengths are increased by a factor of three with the addition of 5% extra PbI_2, with average values for ambipolar diffusion lengths of 330 ± 30 nm for the stoichiometric condition and 920 ± 50 nm with extra PbI_2. Moreover, the lifetime and diffusion lengths obtained with and without extra PbI_2 agree with the values generally extracted from steady state measurements (time-resolved microwave conductivity (TRMC) and steady-state photocarrier grating (SSPG) combined with photoconductivity) and are lower compared to values derived from time-resolved photoluminescence (TRPL) characterization.[35] Levine et al. have shown that the variability in lifetime and diffusion length values is due to the interpretation of the results obtained from different characterization techniques. The lifetime extracted from TRPL measurements is obtained in transient mode and using light intensities orders of magnitude higher than 1 Sun in a very localized spot, therefore potentially leading to different recombination mechanisms. With light intensities comparable to 1 Sun, large area illumination covering the whole sample

Table 1. Table summarizing the parameters extracted from CRPH measurements on $MAPbI_3$ with 0% excess PbI_2 (10% MASCN) and $MAPbI_3$ with 5% excess PbI_2 (5% MASCN). The results are averaged over two samples per condition and the uncertainty corresponds to the standard deviation.

Extra PbI_2	Type	n_0 [cm^{-3}]	μ_n [$cm^2\ V^{-1}\ s^{-1}$]	μ_p [$cm^2\ V^{-1}\ s^{-1}$]	τ [ns]	$L_{D,amb}$ [nm]
0%	*n*	$(1.3 \pm 0.3) \times 10^{11}$	16 ± 6	11 ± 3	3 ± 2	240 ± 90
5%	*n*	$(2.7 \pm 0.1) \times 10^{12}$	14 ± 6	8 ± 4	29 ± 5	700 ± 200

and measurements under steady-state condition, CRPH provides relevant diffusion lengths and lifetimes for solar cells under working conditions.

To confirm the reproducibility of these results, one additional sample for each condition, with data extracted from a distinct substrate, have been measured (see Figures S4 and S5, Supporting Information) and the parameters averaged over the two samples per condition are summarized in **Table 1**. The increase in carrier density is consistent with the n-doping effect of excess PbI_2 previously reported for $MAPbI_3$.[26,27] It is important to note that PbI_2 is highly resistive (conductivity around 10^{-13}–10^{-10} S cm^{-1}) and typically exhibits a p-type character.[48,49] Therefore, it is unlikely that the increase in electron density observed upon excess PbI_2 is due to the presence of the secondary phase itself. The improvement of carrier recombination lifetime by one order of magnitude and diffusion length by a factor of three supports the hypothesis of deep trap passivation. Passivation of grain boundaries by excess PbI_2 has been reported in the literature and seems to be supported by the SEM images showing the formation of PbI_2 phase surrounding the grains.[17,21–23] To determine whether the excess PbI_2 passivates deep traps at the grain boundaries or within the bulk, we further carried out photo-Hall measurements on $MAPbI_3$ films with variable grain size and processed with and without excess PbI_2.

2.2. Evolution with Grain Size and MASCN Addition

$MAPbI_3$ thin films of variable grain size have been processed by tuning the concentration of MASCN additive as well as the annealing temperature.[14] **Figure 5** displays the SEM images of additional films processed for this study and Table S2 in Supporting Information summarizes the MASCN additive concentration and annealing temperature for each film. The SEM image of an additional film processed without PbI_2 is given in Figure S6 (Supporting Information). Under stoichiometric conditions, $MAPbI_3$ thin films are processed with grain sizes ranging from 120 ± 10 nm (Figure 5a) to 600 ± 100 nm (Figure 1a). With the addition of 5% extra PbI_2 in the precursor solution, the grain size is tuned from 220 ± 20 nm to 2.1 ± 0.3 µm (Figure 5c,d). XRD spectra of all films are displayed in Figure S7 (Supporting Information). A peak at 12.7° corresponding to the PbI_2 phase is observed for all samples processed with 5% extra PbI_2 and the peak intensities of the $MAPbI_3$ phase increase with grain size.

CRPH measurements have been carried out for each of the films with different MASCN concentrations and annealing temperatures, and therefore different grain sizes. The equilibrium electron density n_0, electron μ_n, and hole μ_p mobilities, carrier recombination lifetime τ, electron $L_{D,n}$, hole $L_{D,p}$, and ambipolar $L_{D,amb}$ diffusion lengths have been extracted. The photo-Hall measurements and parameter extractions are displayed

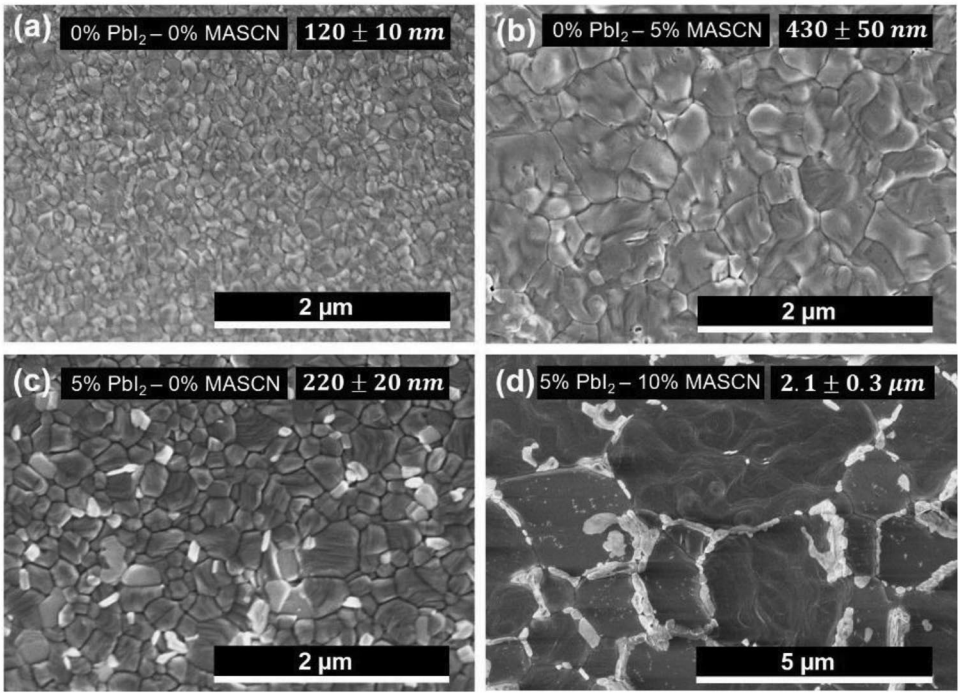

Figure 5. SEM images of $MAPbI_3$ thin films processed with a,b) 0% extra PbI_2 and c,d) 5% extra PbI_2. The MASCN concentration and annealing temperature for each film are given in Table S2 (Supporting Information). Note the different magnification and scale bar in image (d).

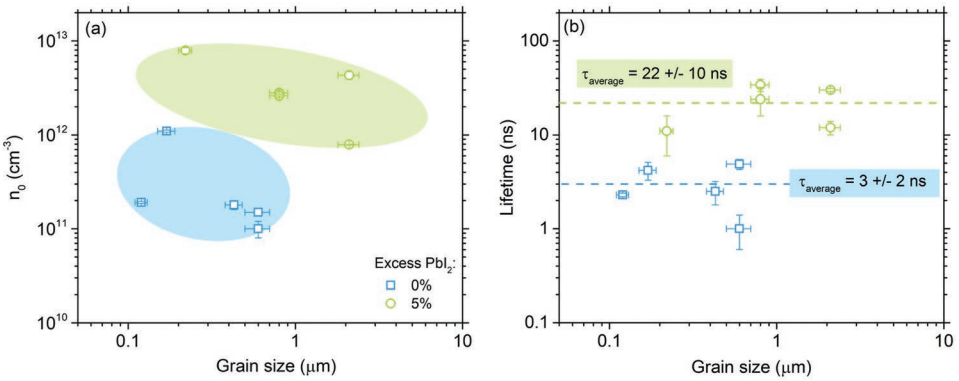

Figure 6. a) Equilibrium (dark) electron density n_0 and b) carrier recombination lifetime τ obtained from carrier-resolved photo-Hall measurements on $MAPbI_3$ thin films of different grain size without and with extra PbI_2.

in Figures S8–S13 (Supporting Information). All samples are n-type and the electron densities n_0 extracted are summarized in **Figure 6**a. Samples processed with 5% extra PbI_2 consistently exhibit an electron density of about one order of magnitude higher than samples processed for the stoichiometric condition (on average), further confirming the doping effect of excess PbI_2. From the data obtained on this set of samples, no trend can be identified in the evolution of electron density with grain size and MASCN concentration in the initial solution (Figure S14, Supporting Information), suggesting that film morphology and MASCN additive concentration have negligible impacts on the intrinsic carrier density. Similarly, the electron and hole mobilities are nominally independent of grain size and MASCN concentration (Figure S15, Supporting Information). From this observation, we can infer that MASCN additive has no measurable impact on carrier density and transport properties of $MAPbI_3$ thin films. While competing and cancelling effects of MASCN and grain size are not impossible, this explanation is unlikely as all optoelectronic parameters remain constant with varying MASCN concentration, both for stoichiometric conditions and for 5% extra PbI_2. This observation is consistent with the hypothesis of essentially complete SCN removal during processing, as previously reported.[14,16] Therefore, the unique role for MASCN in dictating PV device performance likely arises from enhanced film morphology (which can influence deposition of and interaction with other layers of the device structure), as long as it is properly extracted from the final layer using vacuum or annealing treatments. Additionally, grain boundaries evidently do not present substantially detrimental scattering centers, both for the stoichiometric and 5% extra PbI_2 films. These results appear to contradict the work of Reid et al., who show that decreasing grain size leads to a sharp decrease in mobility.[50] However, it is worth noting that this sharp decrease takes place for grain sizes below 100 nm, while the films in the current study exhibit grain sizes above 120 nm (generally the grain size range employed in high-performance photovoltaic devices).

The evolution of carrier recombination lifetime with grain size (Figure 6b) represents key information in the understanding of the PbI_2 passivation effect. If the PbI_2 phase observed in SEM images effectively passivates deep traps situated at the grain boundaries, we would expect the carrier recombination lifetime to be grain size (grain boundary density) dependent for the stoichiometric $MAPbI_3$ films. However, CRPH measurements carried out on samples with four different grain sizes reveal that photocarrier lifetime remains constant with, for example, a value of 2.3 ± 0.1 ns for the smaller grain size of 120 ± 10 nm. This observation agrees with the similar lifetime measured at the grain boundary and at the interior of the grain by Yang et al. using high-resolution confocal fluorescence-lifetime imaging microscopy.[10] Therefore, our results suggest that grain boundaries are relatively benign in $MAPbI_3$ films (i.e., for the synthesis conditions employed and for the range of grain boundary densities considered), as neither the carrier mobilities nor their recombination is influenced by the grain size. The question of recombination induced at the grain boundaries is widely studied for $MAPbI_3$ films leading to contradictory results.[9–12] The absence of consensus may arise from the difficulty to reproduce the processing conditions in different laboratories, as the electronic properties of the grain boundaries could depend on their crystal orientation or on the grain termination chemistry.[32,51] It is also possible that the ability to process compact films with limited trenches separating the grains provides the major factor in achieving benign grain boundaries.[8]

Given the benign nature of the grain boundaries, the impact of excess PbI_2 on recombination must arise either within the grain interiors or at the film surface. However, it is unlikely that extra PbI_2 passivates only surface defects, as the PbI_2 phase mainly resides at the grain boundaries rather than over the entire film surface, according to SEM images. The impact of excess PbI_2 on defects (and recombination) therefore most probably relates to bulk film properties. In this regard, the increase of carrier recombination lifetime with PbI_2 addition can be due to the filling of deep trap states associated with the shift of the Fermi level toward the conduction band. Interestingly, Agiorgousis et al. have used DFT calculation to show that iodine vacancies can create acceptor levels 380 meV below the conduction band edge through the formation of Pb dimers.[31] The evolution of electron densities n_0 extracted in our work suggests a shift of the Fermi level from 430 to 340 meV below the conduction band. Therefore, the n-doping effect of excess PbI_2 may lead to the filling of acceptor states resulting from iodine vacancies or other low-formation-energy defects. The decrease

in carrier recombination lifetime could also be explained by less favorable deep defect formation under the growth conditions (chemical potentials) defined by the excess PbI_2. According to Yin et al., I_{MA} and I_{Pb} are deep point defects, for which formation energy increases from moderate to Pb rich/I poor condition.[24] Nevertheless, with calculated formation energies of 3.01 and 3.45 eV for I_{MA} and I_{Pb}, respectively, under moderate growth conditions, it is unclear if such defects could effectively arise in $MAPbI_3$ processed under stoichiometric conditions.

3. Conclusion

In this work, we use a newly developed carrier-resolved photo-Hall characterization technique to elucidate the impact of additive engineering on n-type $MAPbI_3$ film properties. This technique gives access to both majority and minority carrier properties using one single device and as a function of light intensity or photo carrier injection level. We demonstrate that 5% excess PbI_2 in the precursor solution leads to an improvement of the charge carrier recombination lifetime by an order of magnitude and an increase of the ambipolar diffusion length by a factor of three. Despite the general difficulty of doping lead halide perovskites,[52] we also observe an increase of the electron density by approximately one order of magnitude with 5% excess PbI_2, highlighting the ability to tune the Fermi level position of $MAPbI_3$ by changing the growth conditions (consistent with some previous DFT calculations).[24] A careful study on samples with varying grain sizes further addresses several open questions in the field. First, the relatively constant mobilities and carrier recombination lifetimes with grain size indicate that $MAPbI_3$ grain boundaries are nominally electronically benign, at least under the synthesis conditions tested. These results further suggest that excess PbI_2 more likely passivates defects within the grain interiors (by modifying the growth environment of the grains during formation) rather than at the grain boundaries. The MASCN additive used to tune the grain size is also shown to have no measurable impact on the optoelectronic properties of the $MAPbI_3$ films. This information strengthens the hypothesis of SCN removal during processing, as previously suggested in the literature.[14] Despite the determined relative insensitivity of carrier transport properties to grain boundary density, given facile diffusion of ions along grain boundaries, this parameter is still expected to be important for controlling hysteresis and device environmental/operational stability.[53–56] The ability to obtain high quality films with large compact grains and without pinholes is therefore expected to remain an important target to achieving and maintaining good device performance levels. Finally, these results show the high value of the CRPH approach for more generally addressing questions related to the effectiveness of and mechanisms behind additive engineering within perovskite semiconductors.

4. Experimental Section

Device Fabrication: Hall bars were fabricated by solution processing. Methylammonium iodide (MAI, Dyesol) and lead iodide (PbI_2, 99.99%, TCI chemicals) were dissolved in *N,N*-dimethylformamide (DMF, 99.8%, anhydrous, Sigma-Aldrich) and dimethyl sulfoxide (DMSO, 99.9%, anhydrous, Sigma-Aldrich) with a 9:1 volume ratio at a concentration of 1.25 mol L^{-1}. For the samples with extra PbI_2, the molar concentration of PbI_2 was increased by 5%. When methylammonium thiocyanate (MASCN, Dyesol) additive was used, the powder was directly introduced with the precursors. The concentration given in the main text was in mol% relative to $MAPbI_3$. The solution was stirred at room temperature for 4 h and filtered using PTFE 0.2 µm filters prior to deposition. Glass substrates were sonicated in deionized water, acetone, and isopropanol for 10 min each. Spin-coating was used to deposit the $MAPbI_3$ solution (5000 rpm for 30 s) using chlorobenzene as antisolvent. The antisolvent dripping step played a major role in the quality of the thin film and has been optimized (250 µL dripped after 5 s) and kept constant for all devices. The films were annealed at 60 °C for 20 min. An annealing temperature of 90 °C was used for the devices without MASCN to get rid of the DMSO-related phase. The thicknesses of the layers range from 345 to 400 nm and were measured for each condition using a Bruker Dektak 150 contact profilometer. The Hall bar had six terminals with active area dimension of width × length = 2 × 4 mm as shown in the inset of Figure 2. The Hall bars were patterned using a mask and a scalpel to remove the surrounding perovskite layer. C60 (30 nm) BCP/(5 nm) Ag (100 nm) electrodes were deposited through a shadow mask by thermal evaporation using an Angstrom EvoVac evaporator operating at a base pressure below 2×10^{-6} Torr. The Hall bar was encapsulated with glass using an epoxy glue on the perimeter. The entire fabrication was done in a nitrogen-filled glovebox with oxygen and water levels below 0.1 ppm.

Thin Film Characterization: X-ray diffraction (XRD) spectra were measured using a Panalytical Empyrean powder diffractometer with Cu Kα X-ray source and 45 kV/40 mA operating conditions. Top-view scanning electron microscope (SEM) images were obtained using an Apreo S by ThermoFisher Scientific operated at 2 kV and 25 pA. The average and standard deviation of grain size was determined using the line intercept method in Image J. The grain size was averaged over 20 lines of 3 to 8 µm and using two samples for each condition. UV–vis absorption spectroscopy was carried out with a Shimadzu UV-3600 spectrophotometer. The reflectivity of the Hall bar sample was obtained using an Enlitech QE-R Quantum Efficiency/Reflectivity system with integrating sphere.

Carrier-Resolved Photo-Hall Measurement: A parallel dipole line (PDL) system was used to generate a unidirectional and pure single harmonic ac magnetic field. The master magnet was rotated using a stepper motor typically operated at 0.5 to 1 rpm. A Hall sensor was placed under the master magnet to monitor the oscillating field. The sample was mounted at the center of the PDL system where a magnetic field amplitude of 0.57 T was reached. A detailed description of the PDL Hall system can be found elsewhere.[29] Light illumination using 638 nm (red) laser was used as light source. The light intensity was modulated over eight orders of magnitude using continuous neutral density filters. A wedge lens was used to deflect the light beam onto the sample. A beam splitter was used to simultaneously illuminate the sample and a silicon photodetector, to monitor the photocurrent at various light intensities and to determine the incident absorbed photon density (G_γ) on the sample. A Keithley 2400 Source Meter Unit (SMU) was used as the current source and a Keithley 2001 Digital Multi Meter (DMM) was employed for voltage measurement. A Keithley 7065 Hall switch matrix card with high impedance buffer amplifiers was used for routing the signals between the samples, the SMU and DMM. The current of the silicon photodetector was monitored using a Keithley 617 electrometer. The longitudinal and transverse (Hall) resistance from the Hall bars was measured under repeated light intensity from the maximum brightness to the dark. The analysis of the Hall signal over time was performed using custom-developed software created in Matlab.[57] A Fourier spectral analysis was performed on the Hall resistance after polynomial background subtraction to identify the Hall signal of the same frequency with the reference oscillating magnetic field. Finally software lock-in detection was performed to extract the final Hall signal from the raw Hall resistance traces, using a typical lock-in time constant of 120 s. Additional information on the photo-Hall setup and data analysis can be found elsewhere.[28,29]

Supporting Information

Supporting Information is available from the Wiley Online Library or from the author.

Acknowledgements

This work was supported by the National Science Foundation under Grant No. 1709294 and by the Duke University Energy Initiative Research Seed Fund. The work was performed in part at the Duke University Shared Materials Instrumentation Facility (SMIF), a member of the North Carolina Research Triangle Nanotechnology Network (RTNN), which is supported by the National Science Foundation (Grant ECCS-1542015) as part of the National Nanotechnology Coordinated Infrastructure.

Conflict of Interest

The authors declare no conflict of interest.

Keywords

charge carrier transport, charge recombination, defect passivation, perovskites, photo-Hall characterization

Received: August 19, 2019
Revised: October 15, 2019
Published online: November 12, 2019

[1] M. A. Green, A. Ho-Baillie, H. J. Snaith, *Nat. Photonics* **2014**, *8*, 506.
[2] A. K. Jena, A. Kulkarni, T. Miyasaka, *Chem. Rev.* **2019**, *119*, 3036.
[3] T. Li, Y. Pan, Z. Wang, Y. Xia, Y. Chen, W. Huang, *J. Mater. Chem. A* **2017**, *5*, 12602.
[4] W. A. Dunlap-Shohl, Y. Zhou, N. P. Padture, D. B. Mitzi, *Chem. Rev.* **2019**, *119*, 3193.
[5] Y. Du, H. Cai, H. Wen, Y. Wu, Z. Li, J. Xu, L. Huang, J. Ni, J. Li, J. Zhang, *RSC Adv.* **2016**, *6*, 101250.
[6] H. Do Kim, H. Ohkita, H. Benten, S. Ito, *Adv. Mater.* **2016**, *28*, 917.
[7] W. Nie, H. Tsai, R. Asadpour, A. J. Neukirch, G. Gupta, J. J. Crochet, M. Chhowalla, S. Tretiak, M. A. Alam, H. Wang, *Science* **2015**, *347*, 522.
[8] T. S. Sherkar, C. Momblona, L. Gil-Escrig, J. Ávila, M. Sessolo, H. J. Bolink, L. J. A. Koster, *ACS Energy Lett.* **2017**, *2*, 1214.
[9] J. S. Yun, A. Ho-baillie, S. Huang, S. H. Woo, Y. Heo, J. Seidel, F. Huang, Y. Cheng, M. A. Green, *J. Phys. Chem. Lett.* **2015**, *6*, 875.
[10] M. Yang, Y. Zeng, Z. Li, D. H. Kim, C. Jiang, J. Van De Lagemaat, K. Zhu, *Phys. Chem. Chem. Phys.* **2017**, *19*, 5043.
[11] D. W. de Quilettes, S. M. Vorpahl, S. D. Stranks, H. Nagaoka, G. E. Eperon, M. E. Ziffer, H. J. Snaith, D. S. Ginger, *Science* **2015**, *348*, 683.
[12] R. Long, J. Liu, O. V. Prezhdo, *J. Am. Chem. Soc.* **2016**, *138*, 3884.
[13] H. Uratani, K. Yamashita, *J. Phys. Chem. Lett.* **2017**, *8*, 742.
[14] Q. Han, Y. Bai, K. Z. Du, T. Li, D. Ji, Y. Zhou, C. Cao, D. Shin, J. Ding, A. D. Franklin, J. T. Glass, J. Hu, M. J. Therien, J. Liu, D. B. Mitzi, *Energy Environ. Sci.* **2017**, *10*, 2365.
[15] M. K. Kim, T. Jeon, H. Il Park, J. M. Lee, S. A. Nam, S. O. Kim, *CrystEngComm* **2016**, *18*, 6090.
[16] W. Ke, C. Xiao, C. Wang, B. Saparov, H. S. Duan, D. Zhao, Z. Xiao, P. Schulz, S. P. Harvey, W. Liao, W. Meng, Y. Yu, A. J. Cimaroli, C. S. Jiang, K. Zhu, M. Al-Jassim, G. Fang, D. B. Mitzi, Y. Yan, *Adv. Mater.* **2016**, *28*, 5214.
[17] Q. Chen, H. Zhou, T. Bin Song, S. Luo, Z. Hong, H. S. Duan, L. Dou, Y. Liu, Y. Yang, *Nano Lett.* **2014**, *14*, 4158.
[18] T. J. Jacobsson, E. H. Anaraki, B. Philippe, S. D. Stranks, M. E. F. Bouduban, W. Tress, K. Schenk, J. Teuscher, *J. Am. Chem. Soc.* **2016**, *138*, 10331.
[19] C. Roldán-Carmona, P. Gratia, I. Zimmermann, G. Grancini, P. Gao, M. Graetzel, M. K. Nazeeruddin, *Energy Environ. Sci.* **2015**, *8*, 3550.
[20] Y. C. Kim, N. J. Jeon, J. H. Noh, W. S. Yang, J. Seo, J. S. Yun, A. Ho-Baillie, S. Huang, M. A. Green, J. Seidel, T. K. Ahn, S. Il Seok, *Adv. Energy Mater.* **2016**, *6*, 1502104.
[21] L. Wang, C. McCleese, A. Kovalsky, Y. Zhao, C. Burda, *J. Am. Chem. Soc.* **2014**, *136*, 12205.
[22] D. Shan, G. Tong, Y. Cao, M. Tang, J. Xu, L. Yu, K. Chen, *Nanoscale Res. Lett.* **2019**, *14*, 208.
[23] T. Zhang, N. Guo, G. Li, X. Qian, Y. Zhao, *Nano Energy* **2016**, *26*, 50.
[24] W. J. Yin, T. Shi, Y. Yan, *Appl. Phys. Lett.* **2014**, *104*, 063903.
[25] J. Kim, S. Lee, J. H. Lee, K. Hong, *J. Phys. Chem. Lett.* **2014**, *5*, 1312.
[26] G. Paul, S. Chatterjee, H. Bhunia, A. J. Pal, *J. Phys. Chem. C* **2018**, *122*, 20194.
[27] Q. Wang, Y. Shao, H. Xie, L. Lyu, X. Liu, Y. Gao, J. Huang, *Appl. Phys. Lett.* **2014**, *105*, 163508.
[28] O. Gunawan, S. R. Pae, D. M. Bishop, Y. Virgus, J. H. Noh, N. J. Jeon, Y. S. Lee, X. Shao, T. Todorov, D. B. Mitzi, B. Shin, *Nature* **2019**, *575*, 151.
[29] O. Gunawan, Y. Virgus, K. F. Tai, *Appl. Phys. Lett.* **2015**, *106*, 062407.
[30] Y. Chen, H. T. Yi, X. Wu, R. Haroldson, Y. N. Gartstein, Y. I. Rodionov, K. S. Tikhonov, A. Zakhidov, X.-Y. Zhu, V. Podzorov, *Nat. Commun.* **2016**, *7*, 12253.
[31] M. L. Agiorgousis, Y. Y. Sun, H. Zeng, S. Zhang, *J. Am. Chem. Soc.* **2014**, *136*, 14570.
[32] C. J. Tong, L. Li, L. M. Liu, O. V. Prezhdo, *ACS Energy Lett.* **2018**, *3*, 1868.
[33] Q. Jiang, Z. Chu, P. Wang, X. Yang, H. Liu, Y. Wang, Z. Yin, J. Wu, X. Zhang, J. You, *Adv. Mater.* **2017**, *29*, 1703852.
[34] D. K. Schroder, *Semiconductor Material and Device Characterization*, John Wiley & Sons, Hoboken, New Jersey **2006**.
[35] I. Levine, S. Gupta, A. Bera, D. Ceratti, G. Hodes, D. Cahen, D. Guo, T. J. Savenije, J. Ávila, H. J. Bolink, O. Millo, D. Azulay, I. Balberg, *J. Appl. Phys.* **2018**, *124*, 103103.
[36] W. Huang, S. Sadhu, S. Ptasinska, *Chem. Mater.* **2017**, *29*, 8478.
[37] K. Yan, Z. Wei, T. Zhang, X. Zheng, M. Long, Z. Chen, *Adv. Funct. Mater.* **2016**, *26*, 8545.
[38] J. Endres, D. A. Egger, M. Kulbak, R. A. Kerner, L. Zhao, S. H. Silver, G. Hodes, B. P. Rand, D. Cahen, L. Kronik, A. Kahn, *J. Phys. Chem. Lett.* **2016**, *7*, 2722.
[39] W. Qiu, Z. Xiao, K. Roh, N. K. Noel, A. Shapiro, P. Heremans, B. P. Rand, *Adv. Mater.* **2019**, *31*, 1806105.
[40] J. H. Yang, W. J. Yin, J. S. Park, S. H. Wei, *Sci. Rep.* **2015**, *5*, 16977.
[41] A. Walsh, D. O. Scanlon, S. Chen, X. G. Gong, S. H. Wei, *Angew. Chem., Int. Ed.* **2015**, *54*, 1791.
[42] Y. Rakita, I. Lubomirsky, D. Cahen, *Mater. Horiz.* **2019**, *6*, 1297.
[43] M. B. Johnston, L. M. Herz, *Acc. Chem. Res.* **2016**, *49*, 146.
[44] S. D. Stranks, V. M. Burlakov, T. Leijtens, J. M. Ball, A. Goriely, H. J. Snaith, *Phys. Rev. Appl.* **2014**, *2*, 034007.
[45] X. Wen, Y. Feng, S. Huang, F. Huang, Y. B. Cheng, M. Green, A. Ho-Baillie, *J. Mater. Chem. C* **2015**, *4*, 793.
[46] M. Rosling, H. Bleichner, P. Jonsson, E. Nordlander, *J. Appl. Phys.* **1994**, *76*, 2855.

[47] H. Y. Hsu, L. Ji, M. Du, J. Zhao, E. T. Yu, A. J. Bard, *J. Phys. Chem. C* **2016**, *120*, 19890.
[48] J. Ponpon, M. Amann, *Thin Solid Films* **2001**, *394*, 276.
[49] A. P. Lingras, G. Simkovich, *J. Phys. Chem. Solids* **1978**, *39*, 1225.
[50] O. G. Reid, M. Yang, N. Kopidakis, K. Zhu, G. Rumbles, *ACS Energy Lett.* **2016**, *1*, 561.
[51] J. Haruyama, K. Sodeyama, L. Han, Y. Tateyama, *J. Phys. Chem. Lett.* **2014**, *5*, 2903.
[52] H. Zhang, M. Hou, Y. Xia, Q. Wei, Z. Wang, Y. Cheng, Y. Chen, W. Huang, *J. Mater. Chem. A* **2018**, *6*, 9264.
[53] Y. Shao, Y. Fang, T. Li, Q. Wang, Q. Dong, Y. Deng, Y. Yuan, H. Wei, M. Wang, A. Gruverman, J. Shield, J. Huang, *Energy Environ. Sci.* **2016**, *9*, 1752.
[54] J. S. Yun, J. Seidel, J. Kim, A. Mahboubi, S. Huang, J. Lau, N. J. Jeon, S. Il Seok, M. A. Green, A. Ho-baillie, *Adv. Energy Mater.* **2016**, *6*, 1600330.
[55] G. Grancini, M. K. Nazeeruddin, *Nat. Rev. Mater.* **2019**, 4, 4.
[56] C. C. Boyd, R. Cheacharoen, T. Leijtens, M. D. McGehee, *Chem. Rev.* **2019**, *119*, 3418.
[57] O. Gunawan, M. Pereira, *Rotating Magnetic Field Hall Measurement System* US Patent 9, *772*, 385, **2017**.

